The Astrophysical Journal, 923:176 (11pp), 2021 December 20 https://doi.org/10.3847/1538-4357/ac307c

Simulating Solar Maximum Conditions Using the Alfvén Wave Solar Atmosphere Model (AWSoM)

Nishtha Sachdeva[1], Gábor Tóth[1], Ward B. Manchester[1], Bart van der Holst[1], Zhenguang Huang[1], Igor V. Sokolov[1], Lulu Zhao[1], Qusai Al Shidi[1], Yuxi Chen[1], Tamas I. Gombosi[1], Carl J. Henney[2], Diego G. Lloveras[3], and Alberto M. Vásquez[3,4]
[1] Department of Climate and Space Sciences and Engineering, University of Michigan, Ann Arbor, MI 48109, USA; nishthas@umich.edu
[2] AFRL/Space Vehicles Directorate, Kirtland AFB, NM, USA
[3] Instituto de Astronomía y Física del Espacio, Consejo Nacional de Investigaciones Científicas y Técnicas - Universidad de Buenos Aires, Ciudad de Buenos Aires, CC 67-Suc 28, Argentina
[4] Departamento de Ciencia y Tecnología, Universidad Nacional de Tres de Febrero, Buenos Aires, Argentina
Received 2021 August 18; revised 2021 October 4; accepted 2021 October 14; published 2021 December 21

Abstract

To simulate solar coronal mass ejections (CMEs) and predict their time of arrival and geomagnetic impact, it is important to accurately model the background solar wind conditions in which CMEs propagate. We use the Alfvén Wave Solar atmosphere Model (AWSoM) within the the Space Weather Modeling Framework to simulate solar maximum conditions during two Carrington rotations and produce solar wind background conditions comparable to the observations. We describe the inner boundary conditions for AWSoM using the ADAPT global magnetic maps and validate the simulated results with EUV observations in the low corona and measured plasma parameters at L1 as well as at the position of the Solar Terrestrial Relations Observatory spacecraft. This work complements our prior AWSoM validation study for solar minimum conditions and shows that during periods of higher magnetic activity, AWSoM can reproduce the solar plasma conditions (using properly adjusted photospheric Poynting flux) suitable for providing proper initial conditions for launching CMEs.

Unified Astronomy Thesaurus concepts: Solar wind (1534); Solar corona (1483); Heliosphere (711); Space weather (2037)

1. Introduction

Large-scale eruptions of solar coronal plasma and magnetic fields expelled into the solar wind, so-called coronal mass ejections (CMEs), are major drivers of space weather. When directed toward the Earth, CMEs can lead to severe geomagnetic effects that can threaten the advanced technology that we are highly reliant on. It is therefore important to improve the predictions of their time of arrival at the Earth and of their impact. The first step toward modeling CMEs is to determine the plasma environment these CMEs propagate through.

Many magnetohydrodynamic (MHD)-based models of the solar corona have had success in modeling the solar wind background and propagating CMEs. Various analytical and numerical models developed in the past few decades simulate the solar coronal background (Mikić et al. 1999; Groth et al. 2000; Roussev et al. 2003; Cohen et al. 2007; Feng et al. 2011; Evans et al. 2012), which facilitates the CME propagation to provide predictions. Several coronal models are based on Alfvén wave turbulence, which was discovered some 50 years ago (Coleman 1968; Belcher & Davis 1971). The first physics-based 1D models of the solar corona that include turbulence are Belcher & Davis (1971) and Alazraki & Couturier (1971). These were followed by two-dimensional models (Bravo & Stewart 1997; Ruderman et al. 1998; Usmanov et al. 2000) and more recently three-dimensional (3D) models have been developed (Lionello et al. 2009; Downs et al. 2010; van der Holst et al. 2010) that include Alfvén wave turbulence. The physics processes included in these models have also advanced, with nonlinear interactions between forward-propagating and reflected Alfvén waves to describe coronal heating studied by Velli et al. (1989), Zank et al. (1996), Matthaeus et al. (1999), Suzuki & Inutsuka (2006), Verdini & Velli (2007), Cranmer (2010), Chandran et al. (2011), and Matsumoto & Suzuki (2012). Extended MHD (XMHD) models also include heat conduction, radiative losses, and energy partitioning among particle species as well as temperature anisotropy (Leer & Axford 1972; Chandran et al. 2011; Vásquez et al. 2003; Li et al. 2004; Sokolov et al. 2013; van der Holst et al. 2014). XMHD models are therefore capable of predicting both electron and proton (parallel and perpendicular) temperatures, turbulent wave amplitudes in the solar wind, as well as the wave reflection and dissipation rates. These advances in 3D MHD modeling have provided the capability to study the evolution of the solar wind and solar transients as they propagate from the solar corona into the heliosphere (Kilpua et al. 2017; Manchester et al. 2017; Gombosi et al. 2018, 2021).

Similarly, models have benefited from the increased availability of extensive observational resources such as the Solar Dynamics Observatory/Atmospheric Imaging Assembly (SDO/AIA; Lemen et al. 2012), SDO/Helioseismic Magnetic Imager (SDO/HMI; Schou et al. 2012), Solar Terrestrial Relations Observatory (STEREO; Howard et al. 2008), Solar and Heliospheric Observatory/Large Angle and Spectrometric Coronagraph (SOHO/LASCO; Brueckner et al. 1995), Advanced Composition Explorer (ACE), Wind, and Geotail, which are used to drive and validate these models.

Sachdeva et al. (2019) describes the Alfvén Wave Solar atmosphere Model (AWSoM), a component within the Space

Weather Modeling Framework (SWMF; Tóth et al. 2012; Gombosi et al. 2021), simulations and their validation for solar wind conditions during a period of low solar activity. AWSoM is a 3D extended data-driven MHD model incorporating observational maps of the photospheric magnetic field. Our AWSoM-simulated results for the solar minimum using Air Force Data Assimilation Photospheric Flux Transport—Global Oscillation Network Group (ADAPT-GONG) maps were validated against a comprehensive suite of observations between the low corona and 1 au. AWSoM model results have also been compared to in situ observations from ACE, Wind, and STEREO data at 1 au (Meng et al. 2015; van der Holst et al. 2019) and to observations from Ulysses (Oran et al. 2013; Jian et al. 2016).

In this paper, we continue the work of Sachdeva et al. (2019) and select two Carrington rotations representative of a period of high solar magnetic activity for which to simulate the solar wind plasma background with AWSoM. We discuss the features of the model in the next section and describe the magnetic field maps used for the simulations in Section 2.1. In Sections 2.2 and 2.3 we describe the simulation setup and boundary conditions for the model, respectively. We compare the results of the simulation with observations in the low corona, which includes extreme ultraviolet (EUV) images from SDO/AIA and demonstrate the temperature anisotropy due to energy partitioning within AWSoM. We also compare the solar wind parameters from the model with the observational data from the OMNI database and STEREO-A/B spacecraft. These results are presented in Section 3 followed by a summary in Section 4. The Appendix describes our new approach of splitting the magnetic field in AWSoM.

2. Alfvén Wave Solar Atmosphere Model (AWSoM)

For our work, we apply numerical models developed at the University of Michigan, which are encompassed in the SWMF (Tóth et al. 2005, 2012; Gombosi et al. 2021). The SWMF is a software framework for physics-based space weather modeling and is composed of numerical models that cover a variety of physics domains that can be coupled with each other. In this paper, we use AWSoM to model the solar wind background in the solar corona (SC) and the inner heliosphere (IH) components within the SWMF.

AWSoM (van der Holst et al. 2014) is a self-consistent, 3D global-extended MHD model with its inner boundary at the lower transition region extending into the solar corona and the heliosphere. AWSoM incorporates low-frequency reflection-driven Alfvén wave turbulence, proton temperature anisotropy (parallel and perpendicular proton temperatures), heat conduction, and radiative cooling. The full set of MHD equations are solved using the numerical Block Adaptive Tree Solarwind-Roe-Upwind (BATS-R-US; Powell et al. 1999). The reader is referred to van der Holst et al. (2014) for a complete description of the equations and implementation. Over the years, AWSoM has transitioned from a two-temperature (electrons and ions) model (van der Holst et al. 2010; Jin et al. 2012) to a three-temperature model that accounts for the ion temperature anisotropy (Meng et al. 2015). The energy partitioning scheme in AWSoM has been significantly improved and validated against the data from the Parker Solar Probe (van der Holst et al. 2019, 2021). These improvements include using the critical balance formulation of Lithwick et al. (2007). In van der Holst et al. (2021), the wave period is set to the cascade time of the minor wave at the proton gyroradius scale instead of the major wave resulting in more electron heating and parallel proton heating and less perpendicular proton heating.

Over the years, AWSoM has been extensively validated for both solar minimum and solar maximum activity periods (van der Holst et al. 2010; Meng et al. 2015; Jin et al. 2017; Sachdeva et al. 2019) by comparing the model-simulated results with a variety of observations spanning the low corona and the inner heliosphere. Near the Sun, the simulated density and temperature of the solar corona are compared to reconstructions based on EUV observational data from STEREO-A/B, SDO/AIA, and SOHO/LASCO (Sachdeva et al. 2019). Lloveras et al. (2017, 2020) compared the thermodynamic structure of the AWSoM-simulated quiescent inner solar corona with the tomographic reconstructions of the electron density and temperature using differential emission measure tomography. In the inner heliosphere, AWSoM successfully reproduces the velocity observations of interplanetary scintillation (IPS) data and the in situ solar wind plasma parameters observed at 1 au (Jin et al. 2017; Sachdeva et al. 2019).

2.1. Solar Magnetic Field Maps

AWSoM is a data-driven model and requires the initial radial component of the magnetic field at the inner boundary. Like most solar corona models, this input comes from the solar synoptic/synchronic magnetic field maps, which are essential to drive these models and to make reliable predictions. Consequently, any uncertainties in the photospheric magnetic field measurements impact the near-Sun as well as space weather predictions (Bertello et al. 2014). Worden & Harvey (2000) developed evolving synoptic maps that improve the distribution of magnetic flux on the solar surface while the maps are continuously updated using observations. The ADAPT model (Arge et al. 2010, 2013; Henney et al. 2012) uses the Worden & Harvey (2000) model, which incorporates the effects of solar differential rotation profile, supergranular diffusion, meridional flow, and random emergence of small-scale (background) flux elements to produce synchronic maps. They use the Los Alamos National Laboratory data assimilation code (Arge et al. 2010) to provide multiple realizations, each corresponding to different model parameters and their associated uncertainties. The realizations evolve smoothly over time, independent of each other, without abrupt changes. The changes for any given realization (from one rotation to another) are driven smoothly by different supergranulation flow patterns. ADAPT maps using observations from different instruments are available online from the National Solar Observatory.[5]

In this work, we simulate solar maximum conditions represented by Carrington rotations CR2123 and CR2152, corresponding to the time periods between 2012 April 28 to 2012 May 25 and 2014 June 28 to 2014 July 25, respectively. These rotations are periods when the Sun was populated by strong active regions and enhanced activity. For instance, an M-class flare on 2012 May 17 led to a halo CME eruption during CR2123 (Gopalswamy et al. 2015). Another eruption on 2014 July 8 associated with an M-class flare was observed during CR2152. In Sachdeva et al. (2019), we show a comparison between the solar wind background produced by

[5] https://www.nso.edu/data/nisp-data/adapt-maps

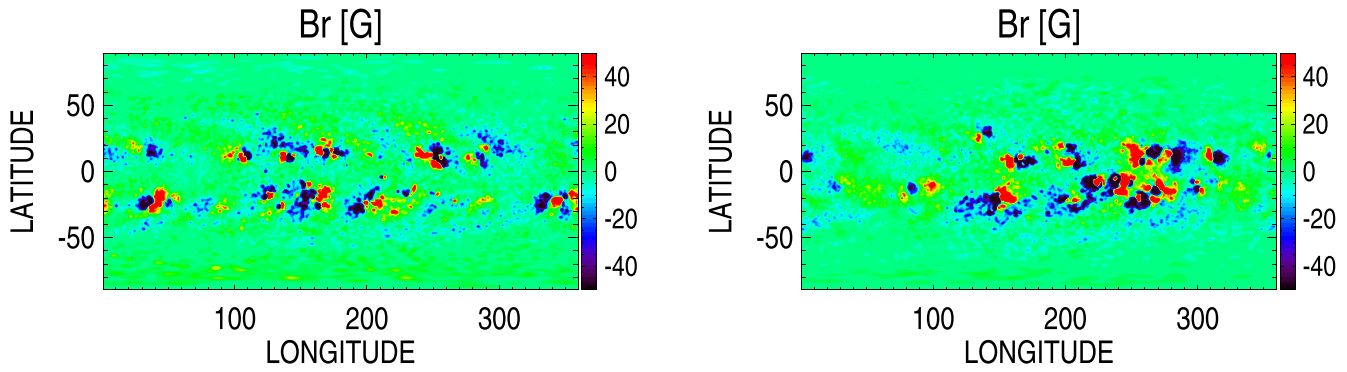

(a) Realization map 01 for CR2123 ADAPT-HMI map (b) Realization map 12 for CR2152 ADAPT-HMI map

Figure 1. Radial magnetic field at $R = 1\ R_\odot$ for (a) CR2123 and (b) CR2152. Realization maps 1 and 12 of the ADAPT-HMI ensemble are chosen for the two rotations, respectively. The radial magnetic field (B_r) in this plot is saturated at ± 50 G.

AWSoM using GONG and ADAPT-GONG magnetograms. The improved results with the ADAPT-GONG maps encourage us to use ADAPT products for our solar maximum runs. We include in this work, for the first time, AWSoM results using ADAPT-HMI maps. Figure 1 shows the input radial magnetic field maps used for CR2123 and CR2152 using ADAPT-HMI maps. The best realization for each of the rotations are chosen based on a quantitative comparison of AWSoM-predicted solar wind parameters (using each realization as the initial condition) with OMNI data at 1 au.

2.2. Boundary Conditions

The magnetic field map is used to set the boundary conditions, in particular the radial component of the magnetic field, at the inner boundary of the spherical grid of AWSoM. For the sake of improved numerical accuracy, the magnetic field $\boldsymbol{B}$ is split into two variables: $\boldsymbol{B}_0$ is an analytic function that matches the boundary conditions, while $\boldsymbol{B}_1 = \boldsymbol{B} - \boldsymbol{B}_0$ is the difference between the numerical solutions of the extended MHD equations and the analytic function. The traditional splitting (Tanaka 1994) requires that $\boldsymbol{B}_0$ is both divergence-free and curl-free, and it does not change in time. Some of these restrictions can be relaxed, and in fact in our previous work $\boldsymbol{B}_0$ was obtained as a potential field source surface (PFSS) solution with the source surface (where the potential field is forced to be radial) set to $R_{ss} = 2.5\ R_\odot$ and the magnetic field continued radially as $\boldsymbol{B}_0(r, \theta, \phi) = \boldsymbol{B}_0(R_{ss}, \theta, \phi)(R_{ss}/r)^2$ for $r > R_{ss}$. This approach results in nonzero curl of $\boldsymbol{B}_0$ at the source surface as well as along the current sheets formed outside the source surface. The nonzero $\boldsymbol{j}_0 = \nabla \times \boldsymbol{B}_0$ is taken into account in the momentum and energy equations (Gombosi et al. 2004).

While this approach is analytically correct, there are some undesirable numerical consequences. The nonzero $\boldsymbol{j}_0$ at the source surface has to be compensated by $\boldsymbol{j} = \nabla \times \boldsymbol{B}_1$, which may lead to inaccuracy in $\boldsymbol{B}_1$ and the total field $\boldsymbol{B}$. Switching from $\nabla \times \boldsymbol{B}_0 = 0$ to a nonzero $\nabla \times \boldsymbol{B}_0$ at the source surface requires a complex algorithm, because for some cells the effect of $\nabla \times \boldsymbol{B}_0$ should be removed, while for other cells it should be added. One can also discretize the effect of $\boldsymbol{B}_0 \times \nabla \times \boldsymbol{B}_0$ in alternative forms (divergence of a Maxwell tensor) and the optimal choice is not obvious.

Our new approach, first used in this work, is to move the source surface outside the domain of the SC model that typically has a radial extent of $24R_\odot$, so we use $R_{ss} = 25\ R_\odot$. This eliminates the nonzero curl of B_0 in the SC domain and minimizes the numerical artifacts. In other words, $\boldsymbol{B}_0$ captures the field near the solar surface and allows accurate representation of the strong fields near the active regions, but it does not need to be representative of the heliospheric current sheet or the helmet streamer. Those features are best captured by the B_1 field obtained by solving the MHD equations.

The PFSS solution can be obtained using either spherical harmonics or the finite difference iterative potential field solver (FDIPS) (Tóth et al. 2011). In this study, we use FDIPS to obtain the PFSS solution for the two rotations. The solution is calculated and stored on a spherical grid that extends from the solar surface at $r = 1\ R_\odot$ to R_{ss}. AWSoM then interpolates this discrete solution to its own nonuniform adaptive grid. We use trilinear interpolation of the $\boldsymbol{B}_{0x}$, $\boldsymbol{B}_{0y}$, and $\boldsymbol{B}_{0z}$ quantities stored on the spherical grid. Using the Cartesian components instead of spherical components avoids issues of interpolation near the poles. With the extended radial domain, using a uniform radial grid to calculate and store $\boldsymbol{B}_0$ is no longer optimal: the required resolution near the solar surface would lead to an excessively large radial grid resolution. To reduce the computational cost (both in storage and calculation time), we switched to a logarithmic radial coordinate, which provides the required accuracy with a similar grid size as we used previously for $R_{ss} = 2.5\ R_\odot$. See the Appendix for more detail.

At the inner boundary, the initial temperature for both isotropic electron and anisotropic (perpendicular and parallel) proton is set to 50,000 K. For the SC model, this selected temperature value in the lower transition region is low enough to generate EUV images without any distortions. This is important for validation efforts of simulated results near the Sun. The selected temperature value is also high enough to not be affected by the complex physical processes in the chromosphere. The proton number density is overestimated and set to 5×10^{18} m^{-3}. This overestimation does not effect the coronal solution (Lionello et al. 2009) and is required to avoid chromospheric evaporation (Sokolov et al. 2013; van der Holst et al. 2014). To avoid a strong density jump at the inner boundary, AWSoM is initialized with an exponentially stratified atmosphere connected to the Parker solution. The temperature profile remains flat while the density falls off exponentially until the effects of radiative cooling are not significant enough to cool the temperature below 50,000 K. As AWSoM relaxes from the initial conditions to the final steady state, the physically meaningful inner boundary moves

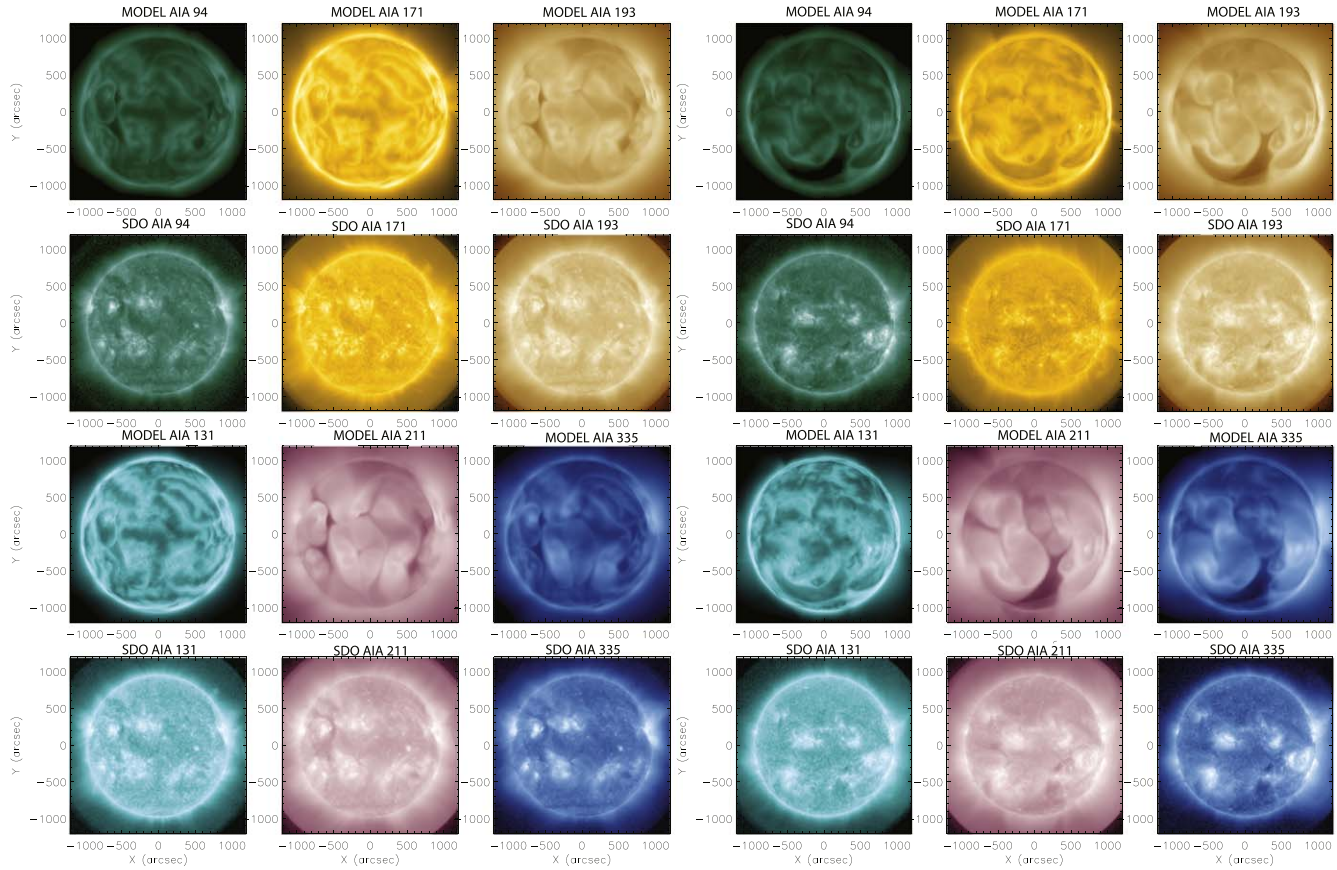

(a) CR2123 (b) CR2152

Figure 2. Comparison between AWSoM-simulated LOS EUV results and SDO/AIA observations for (a) CR2123 and (b) CR2152. The ADAPT-HMI map realizations used for CR2123 and CR2152 are 01 and 12 respectively. Panels (a) and (b) compare the AWSoM LOS (rows 1 and 3) with the SDO/AIA observations (rows 2 and 4) in multiple wavelengths (94, 171, 193, 131, 211, 335 Å).

upwards to where the temperature begins to rise above 50,000 K.

The energy density of the outgoing Alfvén wave is set through the Poynting flux (S_A) of the outward-propagating wave at the inner boundary. AWSoM sets S_A to be proportional to $B_\odot$, the magnetic field strength at the inner boundary (Fisk 1996, 2001; Fisk & Schwadron 2001; Fisk et al. 1999a, 1999b; Sokolov et al. 2013). The proportionality factor $(S_A/B)_\odot$ is an adjustable parameter of AWSoM. From our simulations we find that the stronger magnetic field of the Sun during periods of higher activity requires $(S_A/B)_\odot$ to be lowered compared to 10^6 W m^{-2} T^{-1} used for solar minimum simulations (Sachdeva et al. 2019). The parameter $(S_A/B)_\odot$ in the solar maximum simulations is set to 0.5 and 0.4×10^6 W m^{-2} T^{-1} for CR2123 and CR2152, respectively. Higher Poynting flux leads to a deposition of excess energy density into the chromosphere, which may lead to unphysically high-density peaks at 1 au. We discuss these results later in the paper. The Alfvén wave correlation length ($L_\perp$), which is transverse to the magnetic field direction, is proportional to $B^{-1/2}$ (Hollweg 1986). This proportionality constant ($L_\perp\sqrt{B}$) is an adjustable input parameter in the model that is set to 1.5×10^5 m$\sqrt{T}$. To account for the energy partitioning between electrons and protons, the stochastic heating exponent and amplitude (Chandran et al. 2011) are set to 0.21 and 0.18, respectively.

2.3. Details of the SC–IH Coupling

We use AWSoM to run the SC and IH components of the SWMF. The SC to IH coupling employs a spherical buffer grid between 18–21 $R_\odot$. The SC component uses a 3D spherical grid extending from 1–24 $R_\odot$ and the IH component uses a Cartesian grid that extends from –250 to 250 $R_\odot$with an inner boundary at 20 $R_\odot$ covered by the buffer grid. The SC domain is decomposed into grid blocks consisting of $6 \times 8 \times 8$ grid cells, while IH has $8 \times 8 \times 8$ sized blocks. The grid uses adaptive mesh refinement (AMR). The angular resolution is 1.4° below 1.7 $R_\odot$ and 2.8° in the remaining domain of SC. The cell size in IH ranges between 0.48 $R_\odot$ near the inner boundary and 7.8 $R_\odot$ at the outer boundaries. In addition to the geometric AMR, the current sheet is adaptively resolved with 1.4° resolution in SC and 1 $R_\odot$ resolution in IH. The total number of grid cells in SC and IH are about 4.7 million and 28 million, respectively.

Both SC and IH solve the extended MHD equations in corotating frames, where a steady-state solution can be obtained. The contributions from the Coriolis and centrifugal forces are included into the equations as source terms. Using local time stepping, the SC component is run for 80,000 iterations to get a steady state. Next, SC is coupled with IH for one step followed by 5000 iterations in IH to obtain a steady-state solution in IH as well. We note that the solar wind is superfast magnetosonic in the IH domain, so the solution converges very fast, unlike SC.

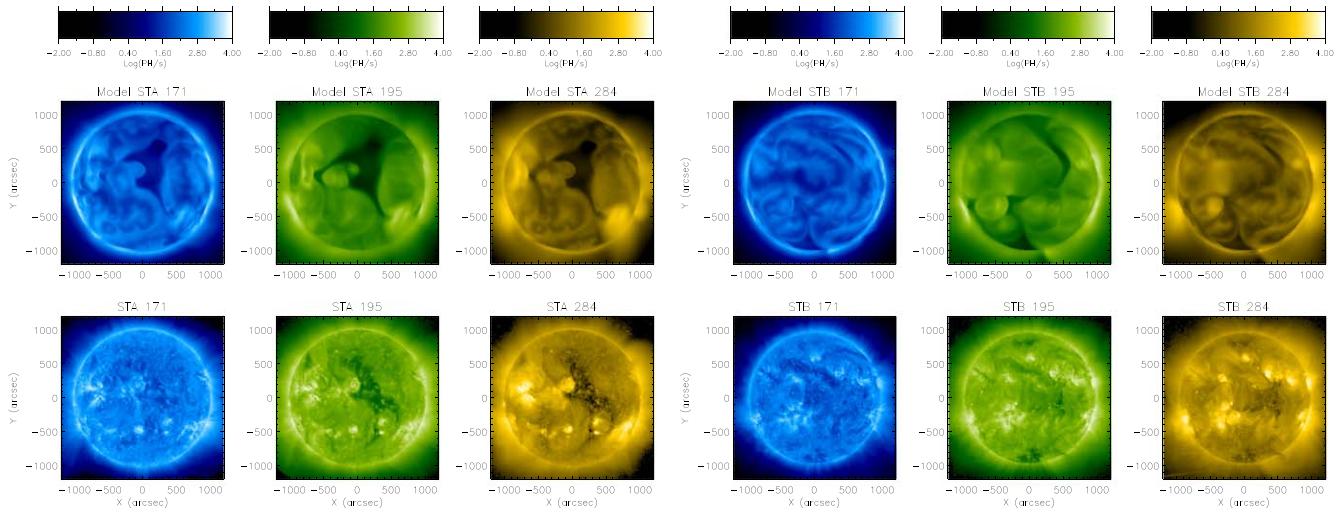

(a) CR2123 STA-EUVI

(b) CR2123 STB-EUVI

(c) CR2152 STA-EUVI

(d) CR2152 STB-EUVI

Figure 3. Data–model comparisons for CR2123 and CR2152 with STEREO-A and -B EUVI observations. Panels (a) and (b) show the comparison between the synthetic EUV images obtained from AWSoM simulation (top row) and the stray-light-corrected observations (bottom row) from STEREO-A and -B respectively in three wavelength channels for CR2123. Panels (c) and (d) show the same comparison for CR2152.

To improve the accuracy of the solution near the Sun, we increase the angular resolution of the grid below 1.7 $R_\odot$ to 0.7° and switch to the fifth-order accurate numerical scheme (Chen et al. 2016) within 1.7 $R_\odot$. The standard second-order shock-capturing scheme (Linde with Koren's limiter) is used in the remainder of the SC region (Tóth et al. 2012). Another 20,000 iterations are performed to relax the solution to the final improved steady state. The improvement is most significant in the synthetic line-of-sight (LOS) EUV images produced by the model. The following section describes the results of the steady-state simulations for the solar maximum conditions using AWSoM.

3. Results

We simulate the background solar wind in the solar corona and the inner heliosphere for Carrington rotations CR2123 and CR2152 using AWSoM and compare the results with data from various observational sources. These rotations are representative of periods of high solar magnetic activity. The physical processes of wave dissipation, heat conduction, and radiative cooling within AWSoM facilitate simulation of the temperature and density structure of the solar corona. AWSoM can produce synthetic EUV images that can be compared with the EUV observations from SDO/AIA and STEREO-EUVI. In the steady-state configuration, the AWSoM model results can be extracted along the trajectories of any given planet/satellite. We compare the simulation output along the STEREO-A/B orbits and also with the solar wind plasma observations from the OMNI database.

Figure 2 shows the AWSoM model simulation output comparison with EUV observations from the SDO/AIA spacecraft. We show the results in six different wavelength channels. Our model reproduces the overall brightness and location of the various active regions quite well. AWSoM does not include any stray-light correction function and the model assumes that for all wavelengths the plasma is optically thin. We see that the coronal holes in the simulation are darker

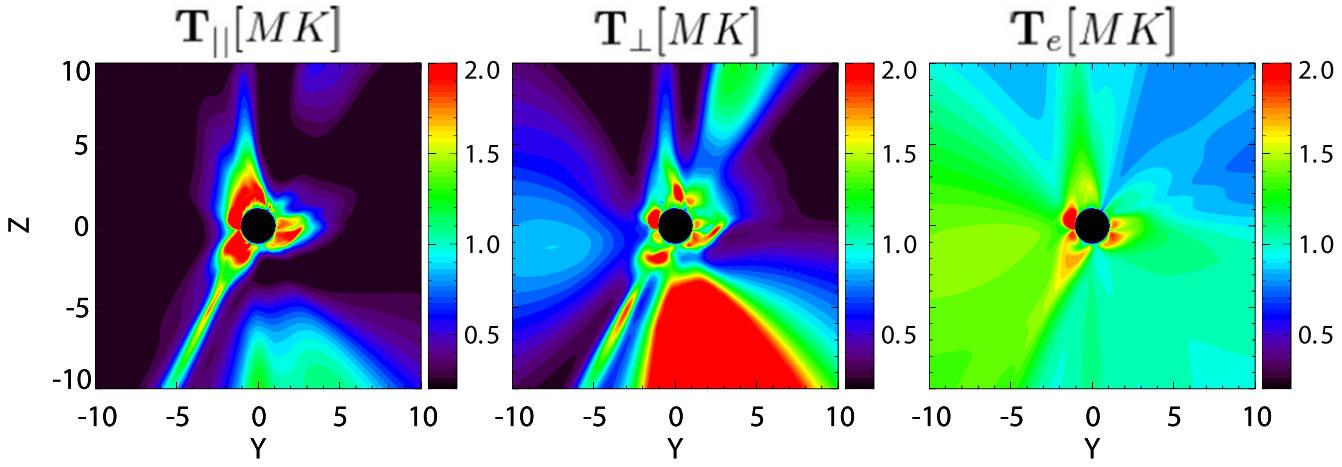

Figure 4. The figure shows the meridional slice ($X = 0$ plane) between -10 *to* 10 $R_{\odot}$ depicting the three temperatures in the low corona. The three panels are the ion temperature parallel to the B field ($T_{||}$), the perpendicular ion temperature ($T_{\perp}$), and the isotropic electron temperature (T_e). All variables are in units of 10^6 K. These results are shown for CR2152.

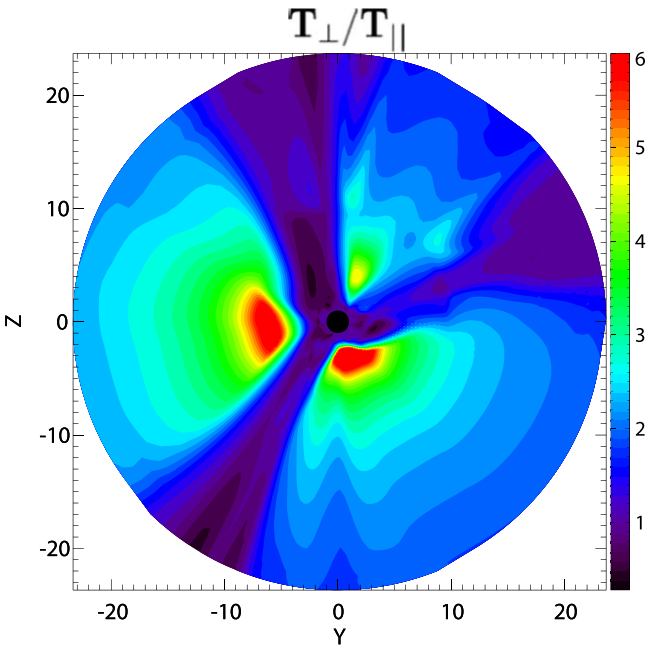

Figure 5. Meridional slice ($X = 0$ plane) in the SC component depicting the ratio of the perpendicular ($T_{\perp}$) and parallel ($T_{||}$) components of ion temperature for CR2152.

compared to the observations, which may in part be due to neglecting the stray-light component caused by long-range scatter in the observations.

Figure 3 shows the comparison of synthetic EUV images obtained from the AWSoM simulation with the STEREO-A/B EUVI observations in three wavelength channels (171, 195, and 284 Å) for both the rotations. The observations have been corrected for stray light due to long-range scattering. In the case of the EUVI detectors, stray light has been shown to significantly contribute to the signal in coronal holes seen on the solar disk and its correction is part of the processing pipeline (Shearer et al. 2012). For CR2123, the STEREO-A and -B spacecraft were separated from Earth by ≈117° and 114° respectively. For CR2152, both the STEREO-A and -B spacecraft were separated from Earth by an angle of ≈162° and located behind the Sun. We see that the location of the coronal holes and the major active regions is reproduced in the model for CR2123. For CR2152, the model does not show the major bright active regions. The overall brightness is comparable with the observations for both the rotations, however we find that not all active regions are as bright in the synthetic EUV images as when observed during solar maximum, and the major coronal holes are darker in the synthetic images.

As described in Section 2, the energy partitioning distributes the heating from the turbulent dissipation in AWSoM over three temperatures. These are the perpendicular and parallel (to the magnetic field) ion temperatures ($T_{\perp}$ and $T_{||}$) and the electron temperature (T_e). Figure 4 shows these temperatures on a meridional slice ($X = 0$ plane) for CR2152. We limit the distance to range between -10 to 10 $R_{\odot}$ in these figures to emphasize the features. Due to highly frequent Coulomb collisions near the Sun, the three temperatures tend to equilibrate, as confirmed by the plots. Further out, the collisions become more infrequent which no longer supports the equilibrium, and the temperatures diverge. The parallel component of ion temperature $T_{||}$ is significant in regions close to the heliospheric current sheet where the plasma beta is high. As we move away from the Sun, stochastic heating leads to an increase in the ion perpendicular temperature $T_{\perp}$. Protons are heated more in the direction perpendicular to the magnetic field in regions away from the Sun and the heliospheric current sheet. The electrons are significantly heated very close to the Sun and around the heliospheric current sheet. Figure 5 shows the ratio of the perpendicular and parallel components of the ion temperature. Near the Sun, the ratio is close to 1 and increases as we move away from the Sun and the heliospheric current sheet.

Figures 6 and 7 present the comparisons between AWSoM simulation results and the observations of solar wind plasma parameters for CR2123 and CR2152. Figure 6 shows the AWSoM results (in red) at the location of the Earth and the solar wind observations from the OMNI database (in black). AWSoM reproduces the steady-state solar wind quite well for both rotations, which represent periods of higher magnetic activity. Overall the model compares reasonably with the observations in predicting the solar wind speed (U_r), proton density (N_p), and temperature at 1 au. AWSoM underestimates the total magnetic field (B) for both rotations. In Figure 6(a) the observations for CR2123 show a high-speed stream around

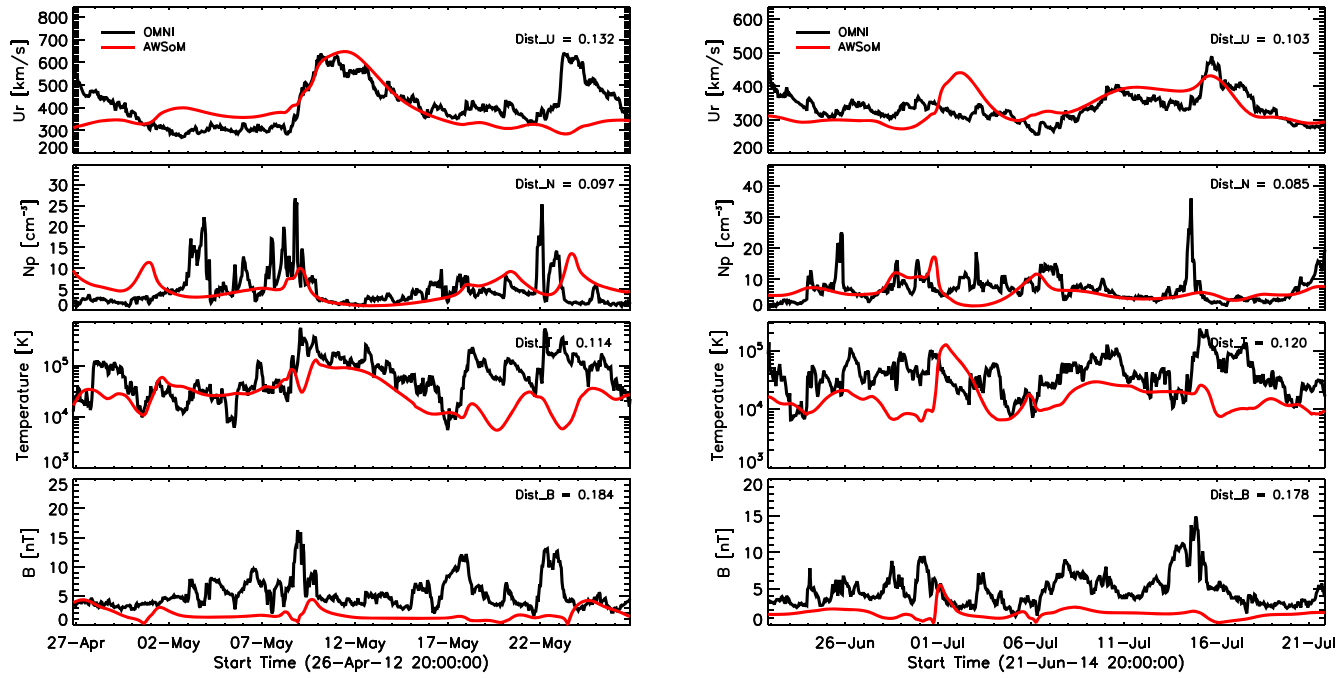

(a) CR2123 (b) CR2152

Figure 6. Data–model comparisons for CR2123 and CR2152 at 1 au. Panels (a) and (b) show the AWSoM results (in red) along the trajectory of the Earth and the solar wind plasma observations from the OMNI database (in black).

2012 May 22 that is completely missed by AWSoM. In Figure 6(b) for CR2152, the simulated output along 1 au shows elevated speeds corresponding to a low-density profile while the observations do not show any such features. Our coronal model is driven by observations of the photospheric magnetic field and not constrained by plasma observations at 1 au. Therefore, not all observed features are always reproduced by the model. Figure 7 shows the same set of plasma parameters observed from STEREO-A and -B. Observational data is shown in black while AWSoM results are shown in red for the two rotations. We find a good comparison between STEREO observations and the AWSoM model results. For both rotations, the model underestimates the proton temperature observed in STEREO-A and -B. The straight black line (between 2014 July 6 and 2014 July 11) in Figure 7(b) is due to partially missing data. In each panel of Figures 6 and 7, we indicate a quantity, Dist, to characterize the error between observations and the model output. Dist is the distance between two curves in a plane independent of the coordinate system so that the temporal and spatial coordinates are treated equally (see Sachdeva et al. 2019 for more detail). We use this quantitative measure to determine the best ADAPT realization out of the 12 available maps for each rotation. The results shown here use the ADAPT map realizations with the smallest distance in solar wind speed (Dist_U) and proton density parameters (Dist_N) between the model and observations.

In our simulations of different phases of the solar cycle, we find that to obtain good comparisons with observations, the Poynting flux $(S_A/B)_\odot$ parameter needs to be modified compared to the optimal values that were used for the solar minimum rotations in Sachdeva et al. (2019). For the solar minimum, the quantity $(S_A/B)_\odot$ was set to 1×10^6 W m^{-2} T^{-1} which provided the best comparisons with various observations. When this value was used for the rotations studied in this paper, the simulations showed unphysical densities at 1 au. The blue line in Figure 8(a) shows the 1 au result for CR2152 using the AWSoM model with $(S_A/B)_\odot = 1$ MW m^{-2} T^{-1}. We see very high density peaks and corresponding low speeds in those simulation results. The red line in the figure shows AWSoM results with $(S_A/B)_\odot$ decreased to 0.4 MW m^{-2} T^{-1} (the same as Figure 6(b)). We conclude that $(S_A/B)_\odot$ needs to be adjusted to reproduce the observed plasma parameters for solar maximum runs with AWSoM. This may also suggest that as the solar cycle tends toward the maximum phase the average magnetic field strength is higher in the solar wind source regions, which requires the amount of Poynting flux per B to be lowered. Z. Huang (2021, in preparation) studies how the Poynting flux parameter $(S_A/B)_\odot$ changes during the last solar cycle and finds that the optimal Poynting flux value for different rotations can be correlated with various characteristics of the solar magnetic field, such as open flux and the area of coronal holes.

The major observational driver of solar corona models, including AWSoM, is the photospheric magnetic field map. There are multiple instruments providing photospheric field measurements and ensembles of magnetograms. However, there are various factors contributing to the uncertainties in these observations including limited observations of the polar regions of the Sun, which requires empirical estimates to fill in the poles. The ADAPT model improves on these magnetic field maps by using data assimilation and including physical processes to compensate for the lack or limitations of observations. We use the ADAPT-GONG and ADAPT-HMI magnetograms for CR2152 to show how the results vary depending on which data product is used with the ADAPT model. Figure 8 shows the AWSoM simulation output at 1 au using ADAPT-GONG (in red) and ADAPT-HMI (in blue) maps. The two simulations have the same model parameters except that the initial (and inner boundary) condition for the radial component of the magnetic field is supplied by ADAPT

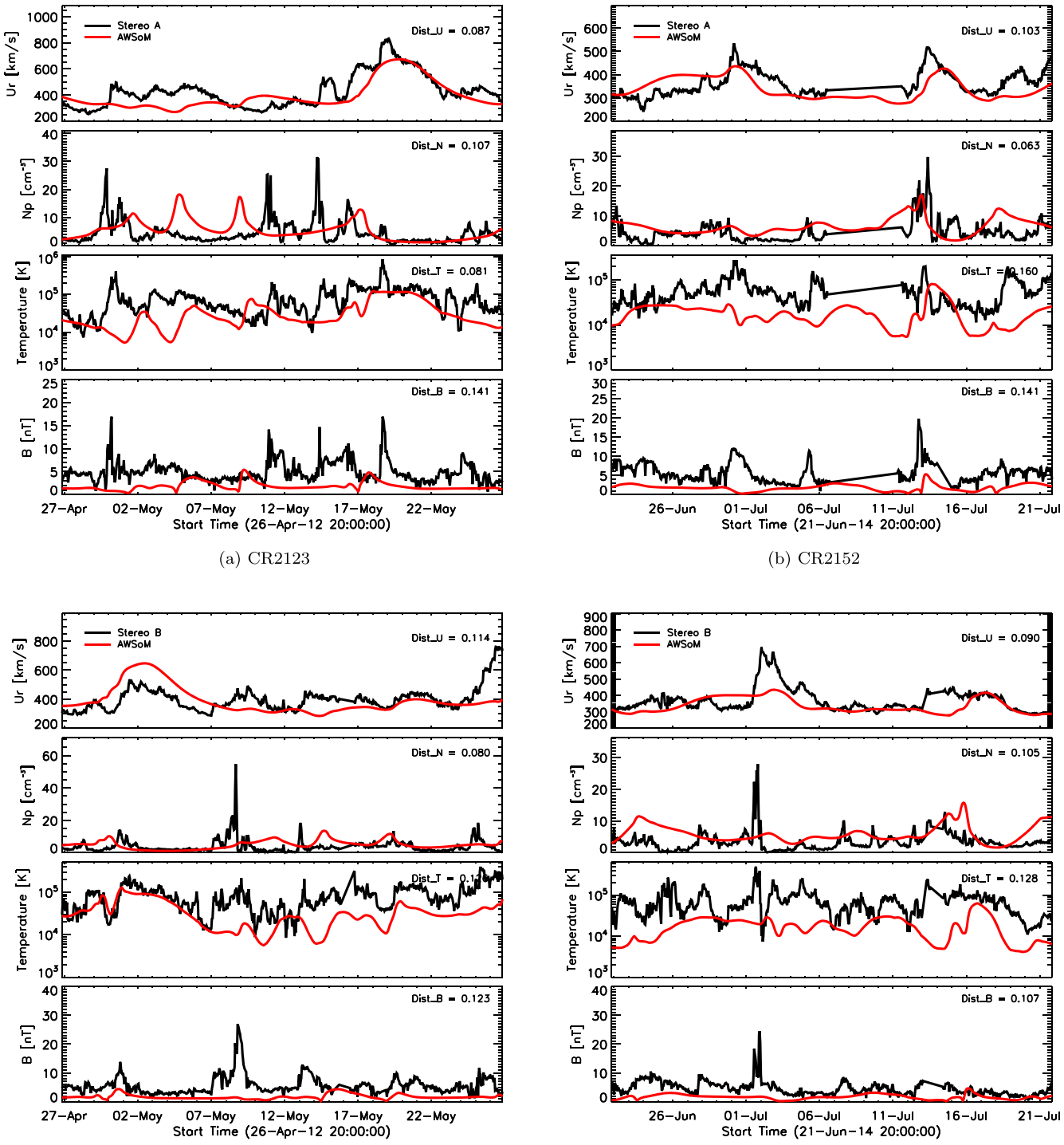

(a) CR2123 (b) CR2152

(c) CR2123 (d) CR2152

Figure 7. Data–model comparisons for CR2123 and CR2152 with STEREO-A and -B observations. Panels (a) and (b) show the AWSoM results (in red) along the trajectory of STEREO-A and the solar wind plasma observations from STEREO-A (in black) for CR2123 and CR2152 respectively. Panels (c) and (d) show the comparisons between AWSoM and STEREO-B data for the two rotations.

maps produced from two different instruments (GONG and HMI). The results demonstrate how the simulation solution varies between the two cases using different magnetograms, as is particularly displayed by the major difference in the proton density at 1 au. The AWSoM output using the ADAPT-GONG map (red) shows a speed profile comparable to the observations while the AWSoM result with ADAPT-HMI (blue) slightly overestimates the speed. However, the lower speed (using ADAPT-GONG) is accompanied by very high density values compared to both the ADAPT-HMI output and observations, which severely impacts the background into which a CME may be launched. The temperature comparison is better in the case of ADAPT-HMI–driven output with AWSoM and the magnetic field prediction is comparable for both cases.

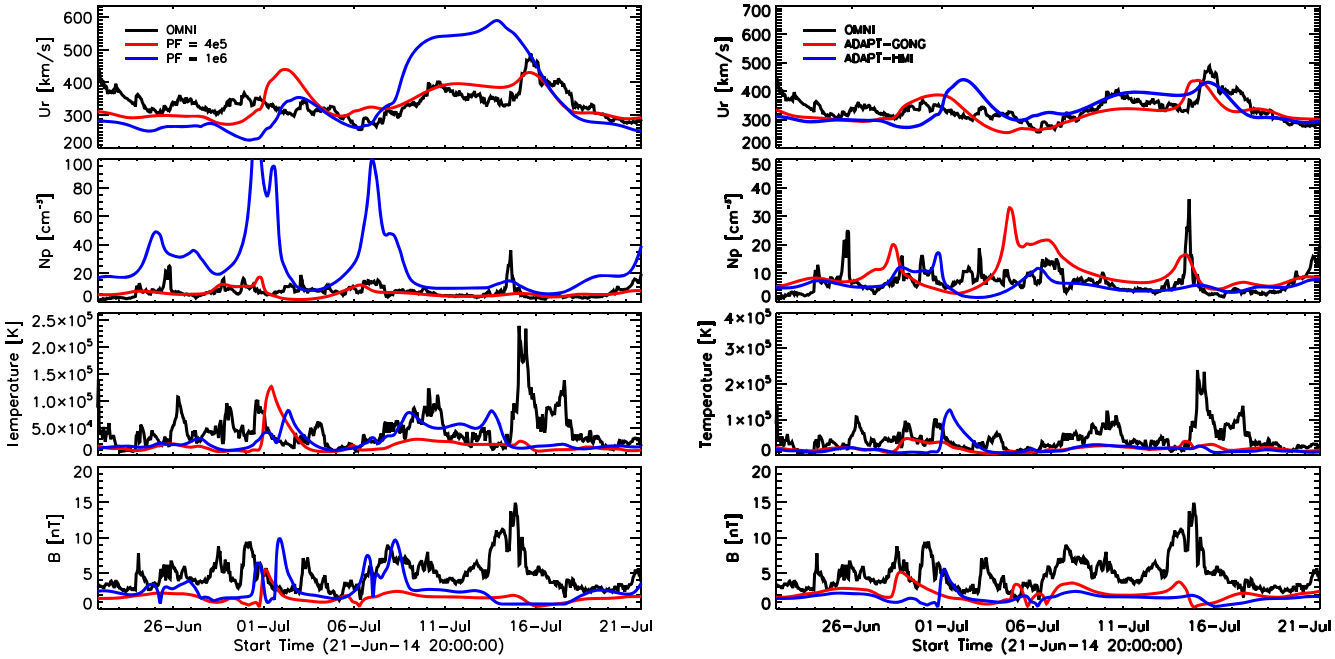

(a) AWSoM results for CR2152 with different values of Poynting Flux per B.

(b) AWSoM results for CR2152 using ADAPT-GONG and ADAPT-HMI magnetograms.

Figure 8. Data–model comparisons for CR2152. Panel (a) shows the AWSoM simulation results at 1 au using different values of the Poynting flux parameter $(S_A/B)_\odot$. The red line corresponds to $(S_A/B)_\odot = 4 \times 10^5$ W m^{-2} T^{-1} (same as Figure 6(b)) and the blue line corresponds to $(S_A/B)_\odot = 1 \times 10^6$ W m^{-2} T^{-1}, which is the optimal value used for solar minimum rotations. Panel (b) shows the AWSoM simulation results using an ADAPT-GONG magnetogram (red line) and an ADAPT-HMI magnetogram (blue line) using the same AWSoM parameters. OMNI data is shown in black.

4. Summary and Discussion

In order to model CMEs and to accurately predict their arrival at and impact on the Earth, it is crucial to first obtain the correct background solar wind solution into which the CMEs can propagate and evolve. Stronger CME events often occur during the phase of the solar cycle when the magnetic activity is high, so it is important to get good background solutions under these conditions. In this work, we chose two Carrington rotations (CR2123 and CR2152) representative of this active time period and perform simulations of the solar corona and the inner heliosphere using the 3D extended MHD model AWSoM. We compare the AWSoM-predicted solar wind to observations of solar corona structure near the Sun and solar wind plasma parameters near the Earth and at STEREO-A and -B.

We use the ADAPT-HMI photospheric magnetic field maps as the observational input to the model for both the rotations. AWSoM simulation results provide the solar coronal temperature and density structure, which are used to produce LOS images comparable to EUV observations. Comparing these synthetic LOS images obtained from AWSoM with the EUV observations from SDO/AIA, we find that our model reproduces the overall brightness, location, and structure of the active regions. Further away from the Sun, we compare the AWSoM-predicted solar wind parameters at 1 au with the in situ spacecraft observations at L1 and by the STEREO-A and -B spacecraft. AWSoM underestimates the background magnetic field, however we get a good match with the speed, proton density, and temperature of the solar wind plasma. Therefore, AWSoM successfully predicts the solar wind background, which is a crucial step toward establishing a plasma environment into which a CME can be propagated and evolved. We also show how different values of the Poynting flux parameter affect the solar wind comparison at 1 au for solar maximum conditions. For the studied solar maximum, the optimal value of $(S_A/B)_\odot$ is about a factor of 2 smaller than the optimal value used for solar minimum conditions. Since most solar corona models are sensitive to the magnetic field observations that are used to drive them, we show how the 1 au simulation results compare with observations and with each other when ADAPT-GONG and ADAPT-HMI maps are used.

This validation work is in preparation for simulating CMEs launched from the surface of the Sun into the background solar wind and studying their evolution and space weather impacts. The good comparisons of AWSoM-simulated solar wind with observations at various radial distances between the Sun and the Earth suggest that our model is capable of reproducing observed solar wind plasma and can be used for space weather modeling and prediction purposes for both solar minimum and solar maximum phases of the solar cycle.

This work was primarily supported by the NSF PREEVENTS grant No. 1663800, the NSF SWQU grant No. PHY-2027555, and by the NASA Heliophysics DRIVE Science Center (SOLSTICE) at the University of Michigan under grant NASA 80NSSC20K0600. W.M. was supported by NASA grants NNX16AL12G and 80NSSC17K0686. We acknowledge high-performance computing support from Cheyenne (doi:10.5065/D6RX99HX) provided by NCAR's Computational and Information Systems Laboratory, sponsored by the NSF, and computation time on Frontera (doi:10.1145/3311790.3396656) sponsored by NSF and the NASA supercomputing system Pleiades. This work utilizes data produced collaboratively between the Air Force Research Laboratory

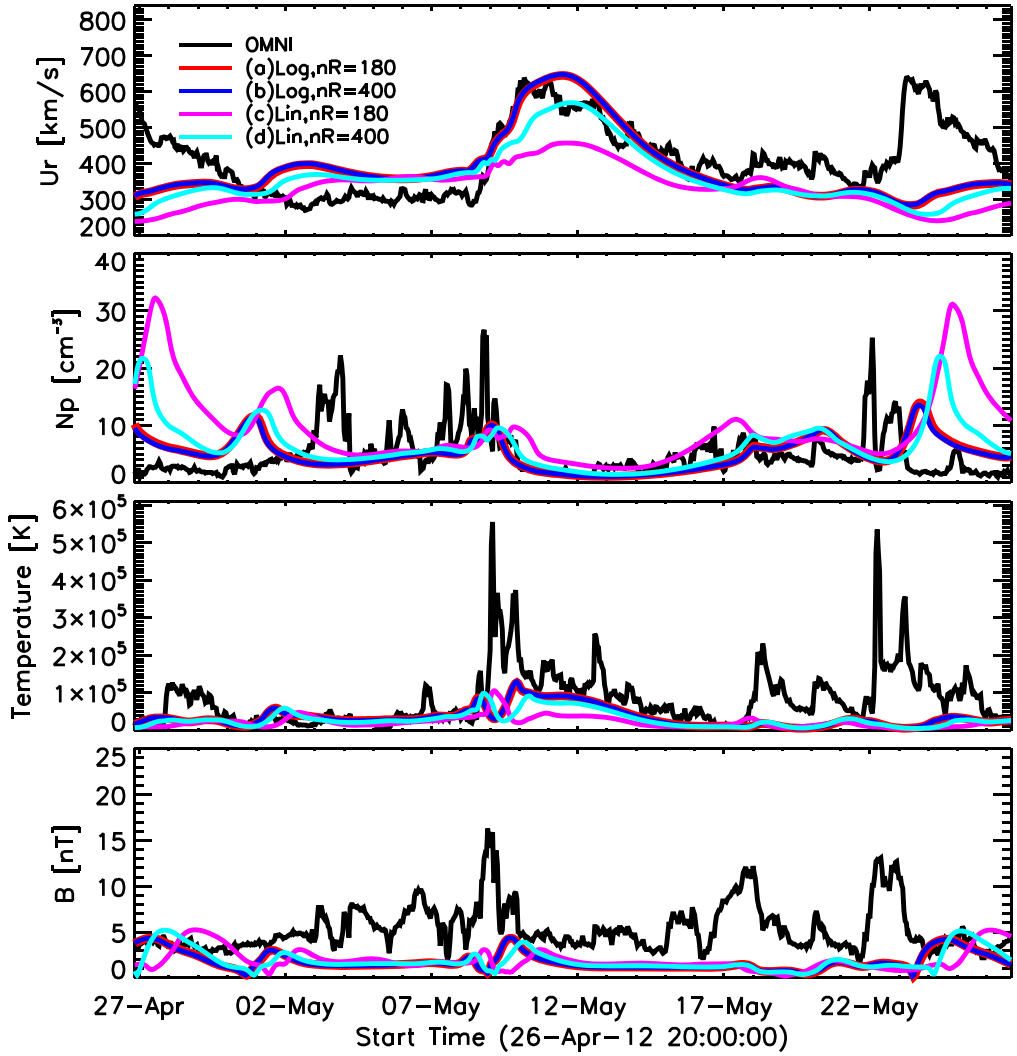

Figure 9. 1 au simulation results using AWSoM for CR2123 for different cases of radial grid and resolution in the PFSS solution. The source surface for the PFSS model is set to 25 $R_\odot$ and the grid is the same in the latitudinal and longitudinal directions for all the results. The red line corresponds to case (a) with a logarithmic scale and $nR = 180$ on the FDIPS grid setup. The line is made thicker for better visibility. Case (b) with a logarithmic scale and $nR = 400$ is represented by the blue line. Cases (c) and (d) correspond to a linear scale and $nR = 180$ and $nR = 400$ in the radial direction, respectively. OMNI data is shown in black.

(AFRL) and the National Solar Observatory. The ADAPT model development is supported by AFRL.

Appendix

In the simulation setup for the PFSS solution, we move the source surface out to 25 $R_\odot$ to prevent nonzero curl of B_0 inside the SC domain and avoid numerical artifacts (Section 2.2). The spherical grid used by the Finite Difference Iterative Potential field Solver (FDIPS; Tóth et al. 2011) extends from the inner boundary at 1 $R_\odot$ to the source surface where B_0 becomes radial. When the source surface radius is large, it is numerically beneficial to use a logarithmic radial grid spacing, since the solution varies fastest near the solar surface and it becomes smoother further out. Figure 9 shows the 1 au simulation output for CR2123 using the AWSoM model for four different cases. For each case, the source surface is set at 25 $R_\odot$, and the FDIPS grid for the PFSS solution is either logarithmic or linear in the radial direction with the number of points in the radial direction (nR) equal to either 180 or 400. The longitudinal and latitudinal resolution is same in all four cases.

In the figure, the red line corresponds to a logarithmic scale with $nR = 180$ in the radial direction (case (a)) and the blue line corresponds to a logarithmic grid with $nR = 400$ (case (b)) (same as Figure 6(a)). The red line is made thicker for better visibility in the plot, because it mostly coincides with the blue line. Next, the pink line corresponds to a linear scale in the radial direction with $nR = 180$ (case (c)) and finally the cyan line corresponds to a linear grid with $nR = 400$ (case (d)). We find that doubling the number of grid points in the radial direction (cases (a) and (b)) does not provide any major advantage as long as the radial grid is logarithmic, so computer memory can be saved by using 180 grid points instead of 400. On the other hand, using a linear radial grid leads to significantly different and inaccurate results (cases (c) and (d)), even for 400 grid points. Although the features in the output are at the same location as for the logarithmic grid, the magnitudes are much lower primarily due to the resolution being not fine enough near the solar surface. We also see an unphysical jump in the density corresponding to very low speeds in cases (c) and (d).

The same source surface radius and the same logarithmic radial grid can also be used to calculate $\boldsymbol{B}_0$ from spherical harmonics and then interpolate to the adaptive grid of AWSoM.

ORCID iDs

Nishtha Sachdeva https://orcid.org/0000-0001-9114-6133
Gábor Tóth https://orcid.org/0000-0001-8459-2100
Ward B. Manchester https://orcid.org/0000-0003-0472-9408
Bart van der Holst https://orcid.org/0000-0001-5260-3944
Zhenguang Huang https://orcid.org/0000-0003-1674-0647
Igor V. Sokolov https://orcid.org/0000-0002-6118-0469
Lulu Zhao https://orcid.org/0000-0003-3936-5288
Qusai Al Shidi https://orcid.org/0000-0003-0426-038X
Yuxi Chen https://orcid.org/0000-0001-7288-2805
Tamas I. Gombosi https://orcid.org/0000-0001-9360-4951
Carl J. Henney https://orcid.org/0000-0002-6038-6369
Diego G. Lloveras https://orcid.org/0000-0003-1402-0398
Alberto M. Vásquez https://orcid.org/0000-0003-3401-6409

References

Alazraki, G., & Couturier, P. 1971, A&A, 13, 380
Arge, C. N., Henney, C. J., González Hernández, I., et al. 2013, in AIP Conf. Proc. 1539, Thirteenth Int. Solar Wind Conf. (Melville, NY: AIP)
Arge, C. N., Henney, C. J., Koller, J., et al. 2010, in AIP Conf. Proc. 1216, Twelfth Int. Solar Wind Conf. (Melville, NY: AIP), 343
Belcher, J. W., & Davis, L., Jr. 1971, JGR, 76, 3534
Bertello, L., Pevtsov, A. A., Petrie, G. J. D., et al. 2014, SoPh, 289, 7
Bravo, S., & Stewart, G. A. 1997, ApJ, 489, 992
Brueckner, G. E., Howard, R. A., Koomen, M. J., et al. 1995, SoPh, 162, 357
Chandran, B. D. G., Dennis, T. J., Quataert, E., & Bale, S. D. 2011, ApJ, 743, 197
Chen, Y., Tóth, G., & Gombosi, T. I. 2016, JCoPh, 305, 604
Cohen, O., Sokolov, I. V., Roussev, I. I., et al. 2007, ApJL, 654, L163
Coleman, P. J. 1968, ApJ, 153, 371
Cranmer, S. R. 2010, ApJ, 710, 676
Downs, C., Roussev, I. I., van der Holst, B., et al. 2010, ApJ, 712, 1219
Evans, R. M., Opher, M., Oran, R., et al. 2012, ApJ, 756, 155
Feng, X., Zhang, S., Xiang, C., et al. 2011, ApJ, 734, 50
Fisk, L. A. 1996, JGR, 101, 547
Fisk, L. A. 2001, JGR, 106, 15849
Fisk, L. A., & Schwadron, N. A. 2001, ApJ, 560, 425
Fisk, L. A., Schwadron, N. A., & Zurbuchen, T. H. 1999a, JGR, 104, 19765
Fisk, L. A., Zurbuchen, T. H., & Schwadron, N. A. 1999b, ApJ, 521, 868
Gombosi, T. I., Chen, Y., Glocer, A., et al. 2021, JSWSC, 11, 42
Gombosi, T. I., Powell, K. G., De Zeeuw, D. L., et al. 2004, CSE, 6, 14
Gombosi, T. I., van der Holst, B., Manchester, W. B., & Sokolov, I. V. 2018, LRSP, 15, 4
Gopalswamy, N., Makela, P., Akiyama, S., et al. 2015, SunGe, 10, 111
Groth, C. P. T., DeZeeuw, D. L., Gombosi, T. I., et al. 2000, JGR, 105, 25053
Henney, C. J., Toussaint, W. A., White, S. M., et al. 2012, SpWea, 10, S02011
Hollweg, J. V. 1986, JGR, 91, 4111
Howard, R. A., Moses, J. D., Vourlidas, A., et al. 2008, SSRv, 136, 67
Jian, L. K., MacNeice, P. J., Mays, M. L., et al. 2016, SpWea, 14, 592
Jin, M., Manchester IV, W. B., van der Holst, B., et al. 2012, ApJ, 745, 6
Jin, M., Manchester IV, W. B., van der Holst, B., et al. 2017, ApJ, 834, 172
Kilpua, E., Koskinen, H. E. J., & Pulkkinen, T. I. 2017, LRSP, 14, 5
Leer, E., & Axford, W. I. 1972, SoPh, 23, 238
Lemen, J. R., Title, A. M., Akin, D. J., et al. 2012, SoPh, 275, 17
Li, B., Li, X., Hu, Y.-Q., & Habbal, S. R. 2004, JGRA, 109, A07103
Lionello, R., Linker, J. A., & Mikíc, Z. 2009, ApJ, 690, 902
Lithwick, Y., Goldreich, P., & Sridhar, S. 2007, ApJ, 655, 269
Lloveras, D. G., Vásquez, A. M., Nuevo, F. A., et al. 2017, SoPh, 292, 153
Lloveras, D. G., Vásquez, A. M., Nuevo, F. A., et al. 2020, SoPh, 295, 76
Manchester IV, W. B., Kilpua, E. K. J., Liu, Y. D., et al. 2017, SSRv, 212, 1159
Matsumoto, T., & Suzuki, T. K. 2012, ApJ, 749, 8
Matthaeus, W. H., Zank, G. P., Oughton, S., et al. 1999, ApJL, 523, L93
Meng, X., van der Holst, B., Tóth, G., & Gombosi, T. I. 2015, MNRAS, 454, 3697
Mikić, Z., Linker, J. A., Schnacl, D. D., et al. 1999, PhPl, 6, 2217
Oran, R., van der Holst, B., Landi, E., et al. 2013, ApJ, 778, 176
Powell, K. G., Roe, P. L., Linde, T. J., et al. 1999, JCoPh, 154, 284
Roussev, I. I., Gombosi, T. I., Sokolov, I. V., et al. 2003, ApJL, 595, L57
Ruderman, M. S., Nakariakov, V. M., & Roberts, B. 1998, A&A, 338, 1118
Sachdeva, N., van der Holst, B., Manchester, W. B., et al. 2019, ApJ, 887, 83
Schou, J., Scherrer, P. H., Bush, R. I., et al. 2012, SoPh, 275, 229
Shearer, P., Frazin, R. A., Hero III, A. O., et al. 2012, ApJL, 749, L8
Sokolov, I. V., van der Holst, B., Oran, R., et al. 2013, ApJ, 764, 23
Suzuki, T. K., & Inutsuka, S.-i 2006, JGRA, 111, A06101
Tanaka, T. 1994, JCoPh, 111, 381
Tóth, G., Sokolov, I. V., Gombosi, T. I., et al. 2005, JGR, 110, A12226
Tóth, G., van der Holst, B., & Huang, Z. 2011, ApJ, 732, 102
Tóth, G., van der Holst, B., Sokolov, I. V., et al. 2012, JCoPh, 231, 870
Usmanov, A. V., Goldstein, M. L., Besser, B. P., & Fritzer, J. M. 2000, JGR, 105, 12675
van der Holst, B., Huang, J., Sachdeva, N., et al. 2021, ApJ, submitted
van der Holst, B., Manchester IV, W. B., Frazin, R. A., et al. 2010, ApJ, 725, 1373
van der Holst, B., Manchester IV, W. B., Klein, K. G., et al. 2019, ApJL, 872, L18
van der Holst, B., Sokolov, I. V., Meng, X., et al. 2014, ApJ, 782, 81
Vásquez, A. M., van Ballegooijen, A. A., & Raymond, J. C. 2003, ApJ, 598, 1361
Velli, M., Grappin, R., & Mangeney, A. 1989, PhRvL, 63, 1807
Verdini, A., & Velli, M. 2007, ApJ, 662, 669
Worden, J., & Harvey, J. 2000, SoPh, 195, 247
Zank, G. P., Matthaeus, W. H., & Smith, C. W. 1996, JGR, 101, 17093